ARTICLE

Vacuum Loss State Monitoring of Aerospace Vacuum Pressure Vessels Based on Quasi-Distributed FBG Sensing Technology

Zhe Gong[1], Ge Yan[2], Jie Ma[1], Chang-Lin Yan[2], Fu-Kang Shen[1], Hu Li[3] and Hua-Ping Wang[1,*]

[1]School of Civil Engineering and Mechanics, Lanzhou University, Lanzhou, 730000, China

[2]Lanzhou Vacuum Equipment Limited Liability Company, Lanzhou, 730000, China

[3]China Yangtze Power Co., Ltd., Yichang, 443000, China

[*]Corresponding Author: Hua-Ping Wang. Email: wanghuaping1128@sina.cn; hpwang@lzu.edu.cn

ABSTRACT

Vacuum pressure vessels are one of the critical components in the aerospace field, and understanding the mechanical behavior feature is particularly important for safe operation. Therefore, it is meaningful to obtain the stress and strain distributions in the key positions of the vacuum tank, which can contribute to the safe performance assessment, operation efficiency, and fault analysis. Hence, this paper provides the distribution characteristics and variation rules of stress and tank strain of vacuum under different internal and external pressures through the elastic theoretical analysis and iteration method. The quasi-distributed fiber Bragg grating (FBG) sensors and the layout on the vacuum pressure vessel have thus been designed to monitor the whole vacuum extraction and loss process under three different loading conditions. Data analysis based on the theoretical results and monitoring information has further been conducted to validate the effectiveness of the proposed monitoring method for possible leakage defects. Research results indicate that the continuously monitoring data can quite sensitively and accurately characterize the microstrain variation features of the vacuum tank at different vacuum stages, and the loading-induced vibration effect should be carefully considered during the data interpretation. The study can provide scientific support for the vacuum loss state monitoring and safe performance assessment of the vacuum pressure vessels.

KEYWORDS

Vacuum loss monitoring; quasi-distributed FBG sensors; theoretical and numerical analysis; strain distribution; vacuum pressure

1 Introduction

The pressure vessel is a special pressure-bearing equipment that can lead to potential leakage and explosion, which has been extensively used in various industries and plays an irreplaceable role [1]. Due to the critical properties of pressure vessels in industrial production, the event of failure or accident may lead to serious injury, environmental pollution, and property losses [2].

Vacuum pressure vessels are widely used in aerospace projects. As one of the key components in the space exploration mission, the vacuum tank plays a crucial role in ensuring a stable vacuum environment. However, due to material fatigue, temperature change, and mechanical vibration, the welded steel tanks

are susceptible to small defects at the weld seams, which can lead to vacuum leakage. The leakage can cause mission failure and equipment damage, which also poses a serious threat to the life safety of astronauts. Pressure vessel accidents in the aerospace field are relatively rare, because the design and manufacturing requirements for pressure vessels are very strict, with careful regular inspection and maintenance measures in the operation. However, relevant cases can still be found in history, such as the US Challenger space shuttle accident. On 28 January 1986, the US Challenger space shuttle exploded and disintegrated 37 s after launch, resulting in the death of seven astronauts. The accident investigation showed that the cause of the accident was the failure of an O-ring, which led to the leakage of liquid oxygen and liquid hydrogen in the fuel tank and caused an explosion. This O-ring was a pressure vessel seal used to ensure the sealing of the fuel tank. The sealing ring lost its elasticity in the low-temperature environment and could not be effectively sealed, resulting in accidents. Therefore, it is necessary to conduct a safety assessment of the pressure vessel structure during service, detect the health and possible leakage, and improve the operational reliability of the equipment [3].

Currently, the safety assessment of pressure vessel structures is mainly based on non-destructive testing techniques. Magnetic particle, penetration, radiation, acoustic emission, ultrasound, infrared thermal imaging technology, and other technologies have been frequently adopted to detect defects, so as to improve the safety and reliability of the equipment and reduce the maintenance costs and downtime of the equipment [4]. Magnetic particle testing has high detection sensitivity, accuracy, and reliability for surface defects, but is not sensitive to deep cracks or internal defects [5]. The penetrant testing process is simple and easy to implement, which is suitable for a wide range of defective surfaces, but insensitive to hidden defects [6]. Radiographic testing has a high detection rate for volumetric defects such as slagging and porosity, but the inspection equipment is expensive and not portable, and the rays may cause injury to the person on-site [6]. Acoustic emission testing can monitor the measured object in real-time online, but it is difficult to distinguish signal and noise [3]. Infrared thermal imaging technology is mainly used for the online detection of heat conduction in high-temperature pressure vessels and the detection of high-stress concentration parts in normal-temperature pressure vessels [7]. It is required that the surface heat absorption rate of the specimen is good, and it is easily affected by temperature and dust. The ultrasonic testing method is easily affected by surface roughness, and the reliability of detection needs to be improved. It can be seen that the above detection techniques only identify the existing defects of specific parts or types of pressure vessels, which are difficult to cover the entire container structure, may miss partial defects, and cannot predict possible faults or damages.

With the rapid development of advanced optical fiber sensing technology and signal demodulation systems, the detection of pressure vessel structures in the service period can be raised to the monitoring level. It means that the real-time, continuous, online monitoring and scientific and fine condition-based maintenance can be realized, and the service life of high-value pressure vessel equipment can be prolonged actively. Optical fiber sensors are widely used in aerospace, oil and gas pipelines, and civil engineering due to their benefits of precise measurement and high sensitivity, small size, lightweight, corrosion resistance, immunity to water and fire, electrical insulation, anti-electromagnetic interference, long term stability, designable, and easy to assemble integrated network [8,9]. Currently, some scholars at home and abroad have adopted optical fiber sensors for temperature and strain measurement and damage identification of pressure vessel structures. Taiwan Scholars used fiber Bragg grating (FBG) sensors for structural strain measurement and crack identification in thin-walled pressure vessel structures [10]. German scholars (2004) used FBG for low-temperature and high-temperature measurements of aerospace pressure vessel structure [11]. Japanese scholars used FBG for on-orbit strain monitoring of aerospace composite pressure vessel structures [12]. Dutch and German scholars used the combined technology of image, acoustic emission, and FBG in the structural health monitoring of composite pressure vessels to continuously monitor and accurately locate damage during the service life, so as to improve the safety of

pressure vessels and reduce maintenance costs [13]. Chinese scholars from Chongqing University used FBG sensors to measure the strain and temperature of composite storage tanks [14], and scholars from Lanzhou University developed a real-time strain field reconstruction and damage and load feature identification method for composite plates based on discrete FBG measurement signals [15]. German scholars used distributed optical fiber for health monitoring of composite pressure vessel structures [16]. Considerable studies on the applicability and reliability of FBG sensors in normal temperature and low-temperature environments have been performed, which provides a theoretical basis for the application of FBG sensors in extreme environments. In terms of application, most of the current research on using FBG sensors to monitor composite tanks is still limited to room temperature conditions. The detailed information and discussion on the mechanical response of different local structures of the tank are not sufficient. A small number of studies have reported the use of FBG to monitor composite fuel tanks in low-temperature environments, but the temperature compensation method has not been clearly described [14]. Based on the above analysis, it is evident that current research mainly focuses on the measurement and damage identification of the local position characteristic parameters of the pressure vessel structure. It can be inferred that the design of a durable optical fiber sensor and its sensing network layout based on the stress analysis of pressure vessel structures can construct the health monitoring system of pressure vessel structures based on optical fiber sensing technology. It can finally contribute to obtaining the continuous state information of pressure vessel structure during the service period, and realizing the damage identification and service safety evaluation of pressure vessel structure according to these massive monitoring data. Furthermore, according to the long-term continuous monitoring information, the functions of maintenance management optimization and remote visual monitoring are realized, which provides important support and scientific guarantee for the safe operation of pressure vessel structure during the service period [17–20].

Therefore, this paper mainly establishes a physical model based on the theory of elastic mechanics and obtains the Lame formula that characterizes the stress and strain of circular pressure vessel structures, so as to understand the stress and strain distribution of pressure vessel tanks under different internal and external pressures. The iteration method has also been used to validate the effectiveness of the theoretical analysis. Considering the vacuum loss process accompanied by the variation of internal and external pressure, the theoretical analysis has been further adapted to instruct the design of the surface-attached FBG sensors and the correlated monitoring system. Three kinds of tests with the vacuum extraction and loss process contained have been carried out, and data analysis has been performed to check the structural information. Discussions based on the monitoring data and theoretical results have also been conducted to declare the strain distribution profiles of the pressure vessel under different loading modes.

2 Vacuum Feature Analysis of Pressure Vessel Structures

2.1 Theoretical Description

For stainless steel vacuum tanks, the vacuum loss process can be considered as a thick-walled cylinder subjected to constant external pressure with decreasing internal pressure. Fig. 1 shows the inner radius R_1, outer radius R_2, cylinder height H, internal pressure P_1, and external pressure P_2 of the thick-walled cylinder, and the cylindrical coordinate system with the z-axis is established. The pressure characteristics of thick-walled pressure vessels without the consideration of thermal stress are: (1) radial stress cannot be ignored and it is in a three-dimensional stress state; (2) the stress distribution in the thickness direction is non-uniform with a stress gradient. For the thick-walled cylinder with internal pressure P_1 and external pressure P_2, a horizontal section is shown in Fig. 2, and the radial stress σ_r, circumferential stress σ_θ, and axial stress σ_z should be solved. Among them, the axial stress σ_z does not change with the height. The tension is positive and compression is negative. For the vessel in the three-dimensional stress state, the shear stress is 0 and the radial stress cannot be neglected. The stress is only referred to the radius. The

circumferential displacement is 0, and just the radial and axial displacements exist. In the analysis, the related unknown parameters will be solved by combining the equilibrium equation, geometrical equation, and physical equation.
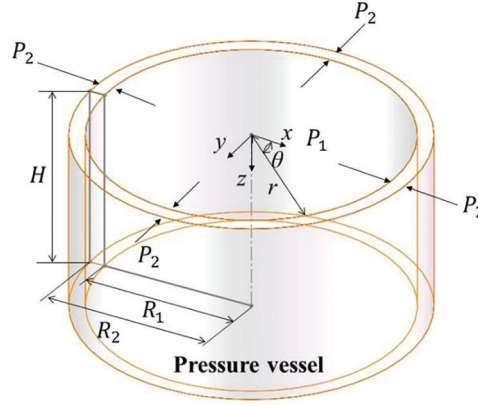

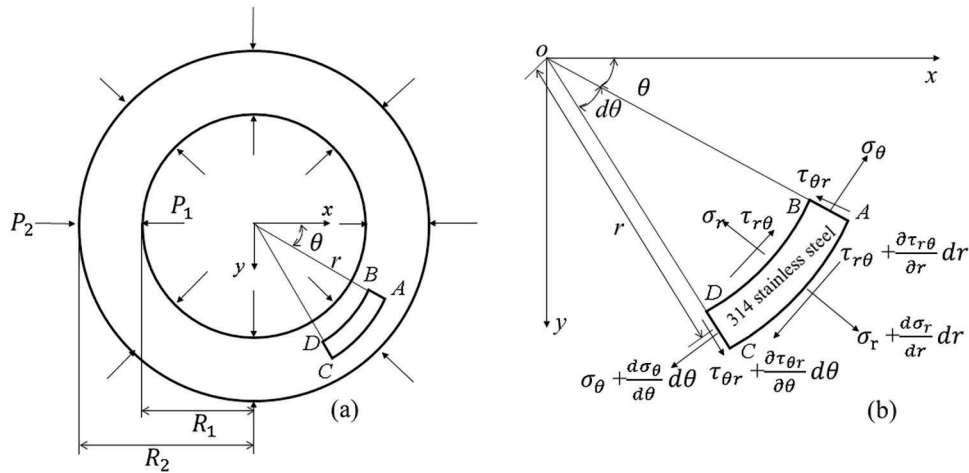**Figure 1:** Refined model of the pressure vessel

Figure 2: Mechanical model of the vacuum tank: (a) Loads and cross-section dimensions of the thick-walled cylinder; (b) Internal stresses of infinitesimal element

(1) Geometrical equation

Radial displacements of the two arc edges in a section with inner radius R_1 and increment dr are marked as u and $u + du$, as shown in Fig. 3. According to the geometrical relationship, radial strain ε_r and circumferential strain ε_θ can be obtained:

$$\varepsilon_r = \frac{(u + du) - u}{dr} = \frac{du}{dr} \tag{1}$$

$$\varepsilon_\theta = \frac{(r + u)d\theta - rd\theta}{rd\theta} = \frac{u}{r} \tag{2}$$
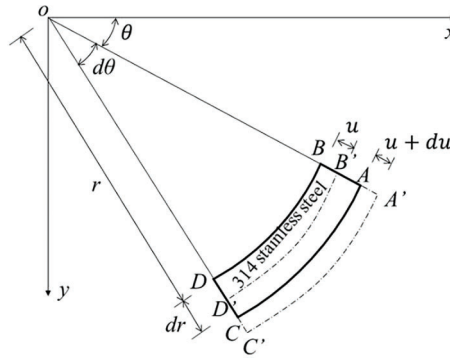
Figure 3: Displacements of infinitesimal element of thick-walled cylinder

The deformation compatibility equation can be obtained by finding the derivative of ε_θ with respect to r:

$$\frac{d\varepsilon_\theta}{dr} = \left(\frac{u}{r}\right)' = \frac{\frac{du}{dr}r - u}{r^2} = \frac{1}{r}\left(\frac{du}{dr} - \frac{u}{r}\right) = \frac{1}{r}(\varepsilon_r - \varepsilon_\theta) \tag{3}$$

(2) Physics equations

According to Hooke's law, the relationship between the components of stress and strain in the cylindrical coordinate system can be expressed as:

$$\varepsilon_r = \frac{1}{E}[\sigma_r - \mu(\sigma_\theta + \sigma_z)] \tag{4a}$$

$$\varepsilon_\theta = \frac{1}{E}[\sigma_\theta - \mu(\sigma_r + \sigma_z)] \tag{4b}$$

$$\varepsilon_z = \frac{1}{E}[\sigma_z - \mu(\sigma_r + \sigma_\theta)] \tag{4c}$$

By subtracting Eq. (4a) from Eq. (4b) by eliminating σ_z, it yields:

$$\varepsilon_r - \varepsilon_\theta = \frac{1+\mu}{E}(\sigma_r - \sigma_\theta) \tag{5}$$

Substituting Eq. (5) into Eq. (3), it gives:

$$\frac{d\varepsilon_\theta}{dr} = \frac{1+\mu}{rE}(\sigma_r - \sigma_\theta) \tag{6}$$

The derivative of ε_θ in Eq. (4b) with respect to r can give birth:

$$\frac{d\varepsilon_\theta}{dr} = \frac{1}{E}\left(\frac{d\sigma_\theta}{dr} - \mu\frac{d\sigma_r}{dr}\right) \tag{7}$$

Uniting Eqs. (6) and (7), it gives:

$$\frac{d\sigma_\theta}{dr} - \mu\frac{d\sigma_r}{dr} = \frac{1+\mu}{r}(\sigma_r - \sigma_\theta) \tag{8}$$

(3) Equilibrium equation

According to the internal force equilibrium condition in the infinitesimal element in Fig. 2b, the following formulas can be obtained:

$$\sigma_\theta - \sigma_r = r\frac{d\sigma_r}{dr} \tag{9a}$$

$$\frac{d\sigma_z}{dz} = 0 \tag{9b}$$

Uniting Eqs. (8) and (9), it gives:

$$r\frac{d^2\sigma_r}{dr^2} + 3\frac{d\sigma_r}{dr} = 0 \tag{10}$$

Eq. (10) is calculated to find σ_r, and then substituted into Eq. (9), which gives:

$$\sigma_r = A - \frac{B}{r^2} \tag{11a}$$

$$\sigma_\theta = A + \frac{B}{r^2} \tag{11b}$$

where A and B are two constants. Two boundary conditions about the radial stress are then introduced:

$$r = R_1, \sigma_r = -P_1 \tag{12a}$$

$$r = R_2, \sigma_r = -P_2 \tag{12b}$$

Substituting Eq. (12) into Eq. (11a), the following expressions can be obtained:

$$A = \frac{P_1R_1^2 - P_2R_2^2}{R_2^2 - R_1^2}, B = \frac{(P_1 - P_2)R_1^2R_2^2}{R_2^2 - R_1^2} \tag{13}$$

Finally, the equilibrium equation in the axial direction is adopted to find σ_z, which is obtained by the internal force equal to the external force:

$$F_i = \sigma_z S = \sigma_z \pi(R_2^2 - R_1^2) \tag{14}$$

$$F_e = \pi R_1^2 P_1 - \pi R_2^2 P_2 \tag{15}$$

where F_i and F_e are internal and external forces, respectively.

Uniting Eqs. (14) and (15), it yields:

$$\sigma_z = \frac{\pi R_1^2 P_1 - \pi R_2^2 P_2}{\pi(R_2^2 - R_1^2)} = \frac{P_1R_1^2 - P_2R_2^2}{R_2^2 - R_1^2} = A \tag{16}$$

Thus, the circumferential, radial and axial stresses in the thick-walled cylindrical structure under internal and external pressures can be obtained by Lame formulas:

$$\sigma_r = \frac{P_1R_1^2 - P_2R_2^2}{R_2^2 - R_1^2} - \frac{(P_1 - P_2)R_1^2R_2^2}{R_2^2 - R_1^2}\frac{1}{r^2} \tag{17}$$

$$\sigma_\theta = \frac{P_1R_1^2 - P_2R_2^2}{R_2^2 - R_1^2} + \frac{(P_1 - P_2)R_1^2R_2^2}{R_2^2 - R_1^2}\frac{1}{r^2} \tag{18}$$

$$\sigma_z = \frac{P_1 R_1{}^2 - P_2 R_2{}^2}{R_2{}^2 - R_1{}^2} \tag{19}$$

By substituting the three stress components into Eq. (4), the radial, circumferential and axial strain components can be calculated:

$$\varepsilon_r = \frac{1}{E}\left((1-2\mu)\frac{P_1 R_1{}^2 - P_2 R_2{}^2}{R_2{}^2 - R_1{}^2} - (1+\mu)\frac{(P_1 - P_2)R_1{}^2 R_2{}^2}{R_2{}^2 - R_1{}^2}\frac{1}{r^2}\right) \tag{20}$$

$$\varepsilon_\theta = \frac{1}{E}\left((1-2\mu)\frac{P_1 R_1{}^2 - P_2 R_2{}^2}{R_2{}^2 - R_1{}^2} + (1+\mu)\frac{(P_1 - P_2)R_1{}^2 R_2{}^2}{R_2{}^2 - R_1{}^2}\frac{1}{r^2}\right) \tag{21}$$

$$\varepsilon_z = \frac{1}{E}\left((1-2\mu)\frac{P_1 R_1{}^2 - P_2 R_2{}^2}{R_2{}^2 - R_1{}^2}\right) \tag{22}$$

2.2 Stress and Strain Distributions under Different Working Conditions

Taking the vacuum tank with sizes of ϕ 400 mm × 700 mm × 5 mm as an example, the physical object is shown in Fig. 4. The specific calculation parameters are listed in Table 1. The stress and strain distribution characteristics of the pressure vessel under different internal and external pressures can thus be figured out according to the derived formulas. It is considered that the actual pressure vessel structure is in an initially non-stress state subjected to atmospheric pressure, and then the corresponding initial stresses and strains are 0. Therefore, the initial non-stress state of the pressure vessel structure is equivalent to the mechanical model under the working condition that both the internal pressure P_1 and the external pressure P_2 of the thick-walled cylindrical structure are 0. The vacuum state is equivalent to the condition that the internal pressure decreases from 0 Pa to −0.1 MPa and the external pressure remains 0. As a result, the stress and strain distributions of the vacuum tank along with the wall thickness can be obtained, as shown in Figs. 5–8.

Figure 4: Physical photo of the vacuum tank

Table 1: Values of the geometrical and mechanical parameters

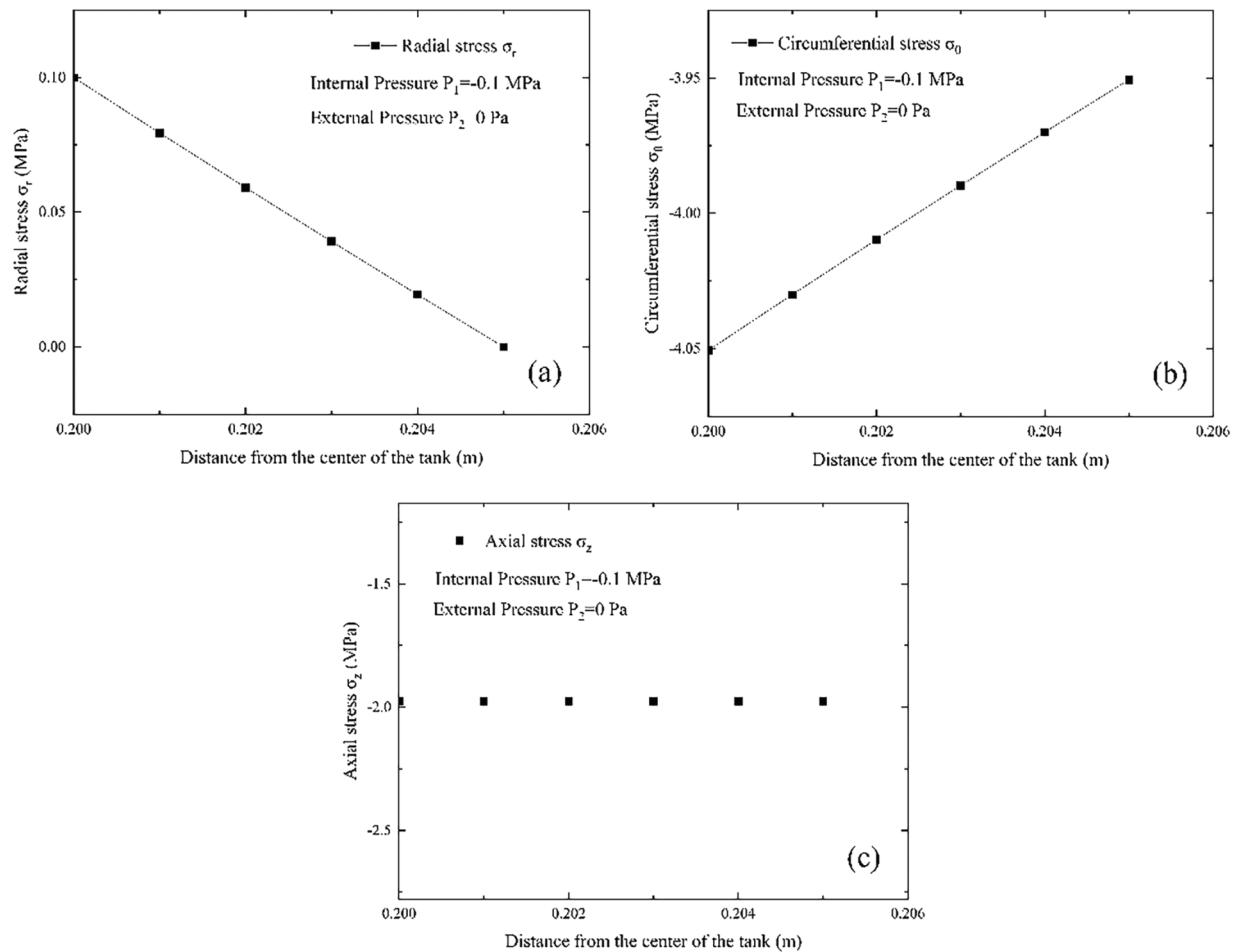| Catalogue	Label	Value	Unit
Inner radius	R_1	0.2	m
Outer radius	R_2	0.205	m
Internal pressure	P_1	−0.1	MPa
External pressure	P_2	0	MPa
Elastic modulus	E	200	GPa
Poisson's ratio	μ	0.3	

Figure 5: Stress distribution characteristics of the vacuum tank under the pressure $P_1 = -0.1$ MPa: (a) Radial stress; (b) Circumferential stress; (c) Axial stress

Fig. 5 shows the distribution of radial stress, circumferential stress and axial stress along the thickness direction of the vacuum tank with size of ϕ 400 mm × 700 mm × 5 mm under the internal pressure of −0.1 MPa. When the distance to the center of the tank varies from the inner diameter of 0.2 m to the

outer diameter of 0.205 m, the radial stress gradually reduces from 0.1 MPa to 0, the circumferential stress increases from −4.05 to −3.95 MPa, and the axial stress remains unchanged with the value of −1.98 MPa, which conforms to the mechanical law.
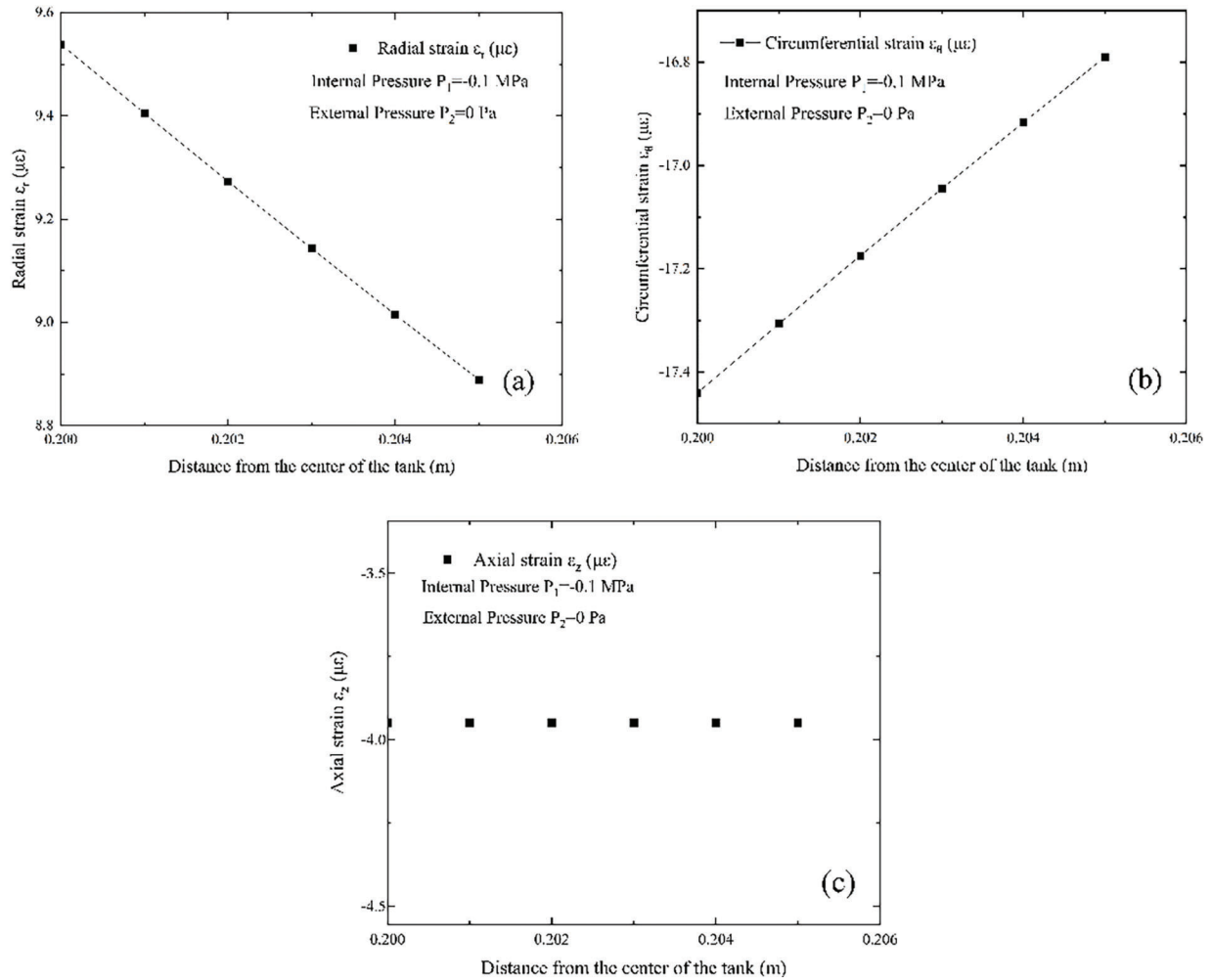

Figure 6: Strains distribution characteristics of the vacuum tank under the pressure $P_1 = -0.1$ MPa: (a) Radial strain; (b) Circumferential strain; (c) Axial strain

Fig. 6 shows the distribution of radial strain, circumferential strain and axial strain along the thickness direction of the vacuum tank with size of ϕ 400 mm × 700 mm × 5 mm under internal pressure of −0.1 MPa. Therefore, when the distance to the center of the tank varies from the inner diameter of 0.2 m to the outer diameter of 0.205 m, the radial strain gradually decreases from 9.53 to 8.88 με, circumferential strain increases from −17.42 to −16.77 με, axial strain keeps stable with the value of −3.95 με. The comparison of Figs. 5 and 6 indicates that the variation principles of the stresses and strains are the same. Therefore, in practical testing, the measured strain information can be used to diagnose the physical state of the vacuum tank structure.
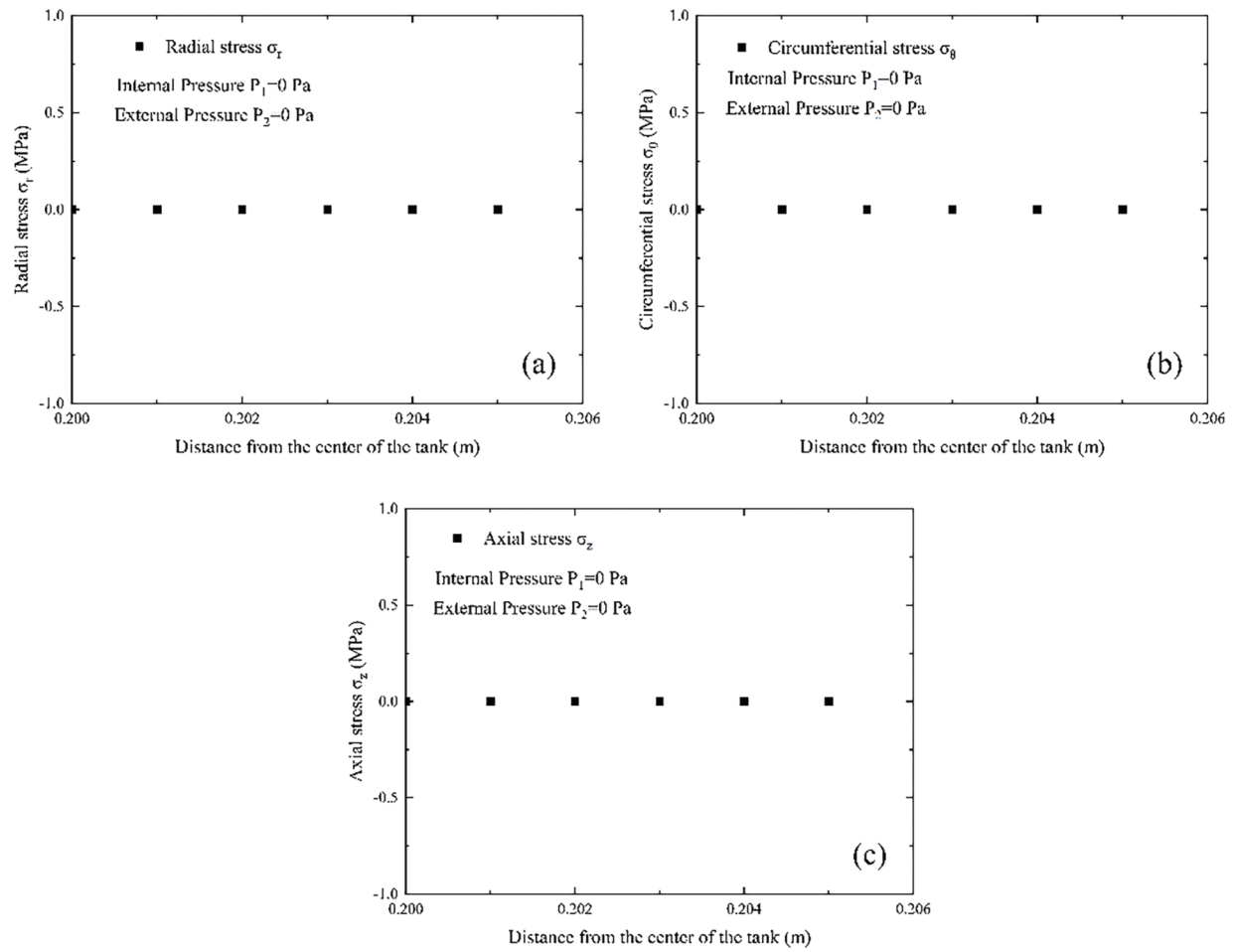
Figure 7: Stress distribution characteristics of the vacuum tank under the pressure $P_1 = 0$ Pa: (a) Radial stress; (b) Circumferential stress; (c) Axial stress
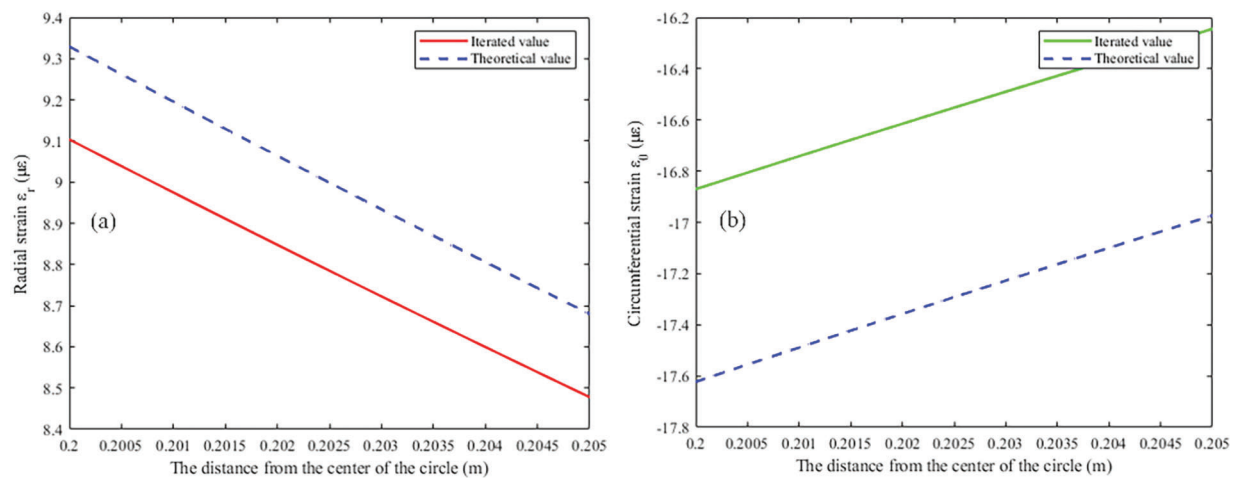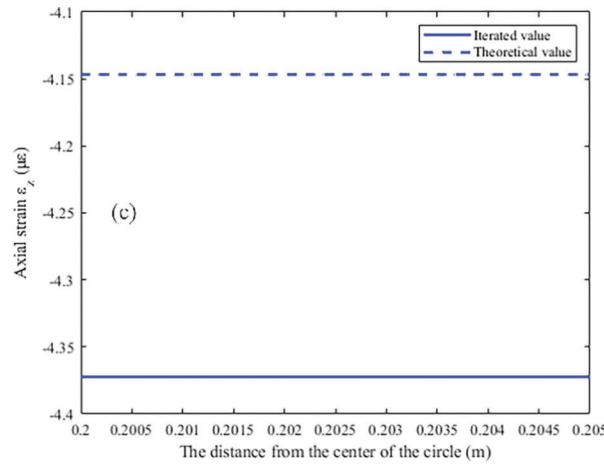

Figure 8: (Continued)

Figure 8: Comparison of iterative solution and theoretical solution: (a) Radial strain; (b) Circumferential strain; (c) Axial strain

Fig. 7 shows the relationship between radial stress, circumferential stress, axial stress and wall thickness of a vacuum tank with the size of ϕ 400 mm × 700 mm × 5 mm without internal or external pressures. It is apparent that when the center distance of the tank is gradually expanded from the inner radius of 0.2 m to the outer radius of 0.205 m, the three-dimensional stress values are 0, which corresponds to the initial non-stress state. Similarly, according to Hooke's law and Eq. (4), the three-dimensional strains corresponding to this loading condition are also 0. When both the internal and external pressures are 0, the radial, circumferential and axial strains of the vacuum tank are 0 at each point, which is in accordance with the assumption of the initial non-stress state.

2.3 Iterative Method

Considering that the subsequent research will involve the vacuum pressure vessel with local micro-defects induced vacuum loss state, it may be difficult to obtain the theoretical analytical solution of the corresponding mechanical model. As a result, there is a need to develop a numerical approach to solving this problem. For this reason, the iterative method is used for the solution calculation of this physical model and comparison with the theoretical analytical solution is also analyzed. σ_r is replaced by σ_r, and then Eq. (10) is iteratively calculated in fourth-order Runge-Kutta format, which gives the control equation:

$$ry'' + 3y' = 0 \tag{23}$$

Transforming Eq. (23) into a first-order form, it yields:

$$\begin{aligned} y_1\prime &= y_2 \\ y_2\prime &= -3y_2/r = f(x,y) \end{aligned} \tag{24}$$

The iterative equation considers the first-order equation:

$$\begin{aligned} y_{n+1} &= y_n + \frac{h}{6}(K_1 + 2K_2 + 2K_3 + K_4) \\ K_1 &= f(x_n, y_n) \\ K_2 &= f\left(x_{n+1/2}, y_n + \frac{h}{2}K_1\right) \\ K_3 &= f\left(x_{n+1/2}, y_n + \frac{h}{2}K_2\right) \\ K_4 &= f(x_{n+1}, y_n + hK_3) \end{aligned} \tag{25}$$

The numerical solution can be obtained by substituting the relevant parameters into Eq. (25). Therefore, the comparison between the numerical strains and the analytical strains is shown in Fig. 8. At the same time, the influence of different step length h on the calculation results is discussed, and the values of ε_r are used for checking the accuracy, which produces Fig. 9. It can be seen that the numerical results are very close to the theoretical analytical solution, and the different step sizes have no effect on the accuracy improvement of the calculation results.
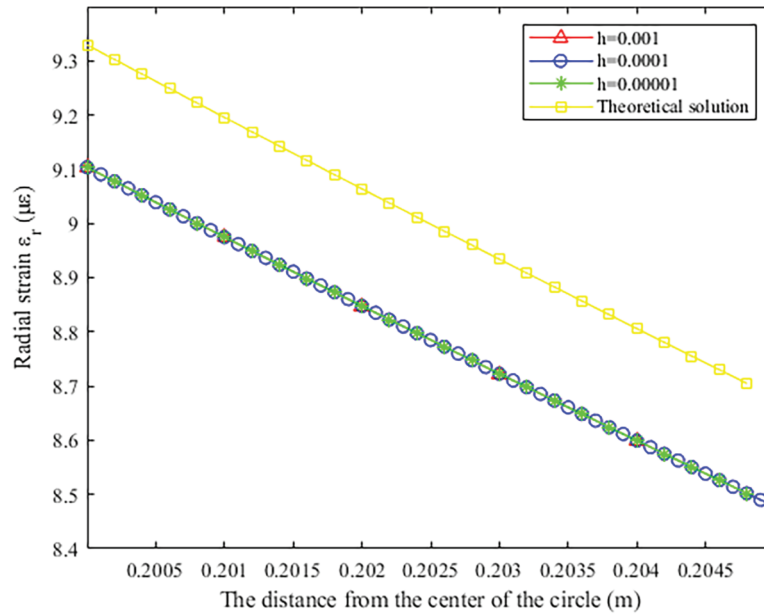

Figure 9: Comparison of radial strain under different step sizes with theoretical solution

It is preliminarily estimated that the error is due to the use of the secant slope at $r = 0.2$ m instead of the exact derivative. The exact derivative $y2(1) = -20.73233$ of the radial stress at 0.2 m calculated by the analytical solution is replaced to obtain Fig. 10. It can be seen that the three-dimensional strain diagrams obtained by numerical calculation are almost completely consistent with the theoretical solution. Thus, the error of the results calculated by the iterative program is due to the assumption that the value at $r = 0.2$ m is not close to the exact derivative. Therefore, in the numerical calculation of complex models, when the theoretical analytical solution cannot be obtained, a much accurate numerical substitution can be obtained by the testing method, so as to realize the numerical calculation and state evaluation of complex physical models.

3 Vacuum Process Monitoring Based on FBG Sensing Technology

3.1 Experimental Description

During the vacuum evacuation process, the internal and external pressures of the pressure vessel are unbalanced with external pressure greater than internal pressure. Therefore, the vessel structure mainly undergoes shrinkage deformation. The process of vacuum loss means that the internal pressure is gradually approaching the external pressure, and the internal and external pressures are gradually reaching an equilibrium state. In addition, the shrinkage deformation of the vessel structure gradually decreases and reaches a certain equilibrium value. According to the aforementioned theoretical analysis, the vacuum pressure vessel has no initial stress in the atmospheric environment, and the vacuum process is correlated

to the case that the internal pressure is decreasing, which leads to the vacuum pressure vessel contracting and suffering from pressure strain. On the other hand, the vacuum loss process means that the internal pressure is increasing, and finally comes to the balance with the external pressure (i.e., initial non-stress state with the assumption that the external pressure is 0). The compression strain also gradually decreases and restores to the initial state that both the stress and strain values are 0.
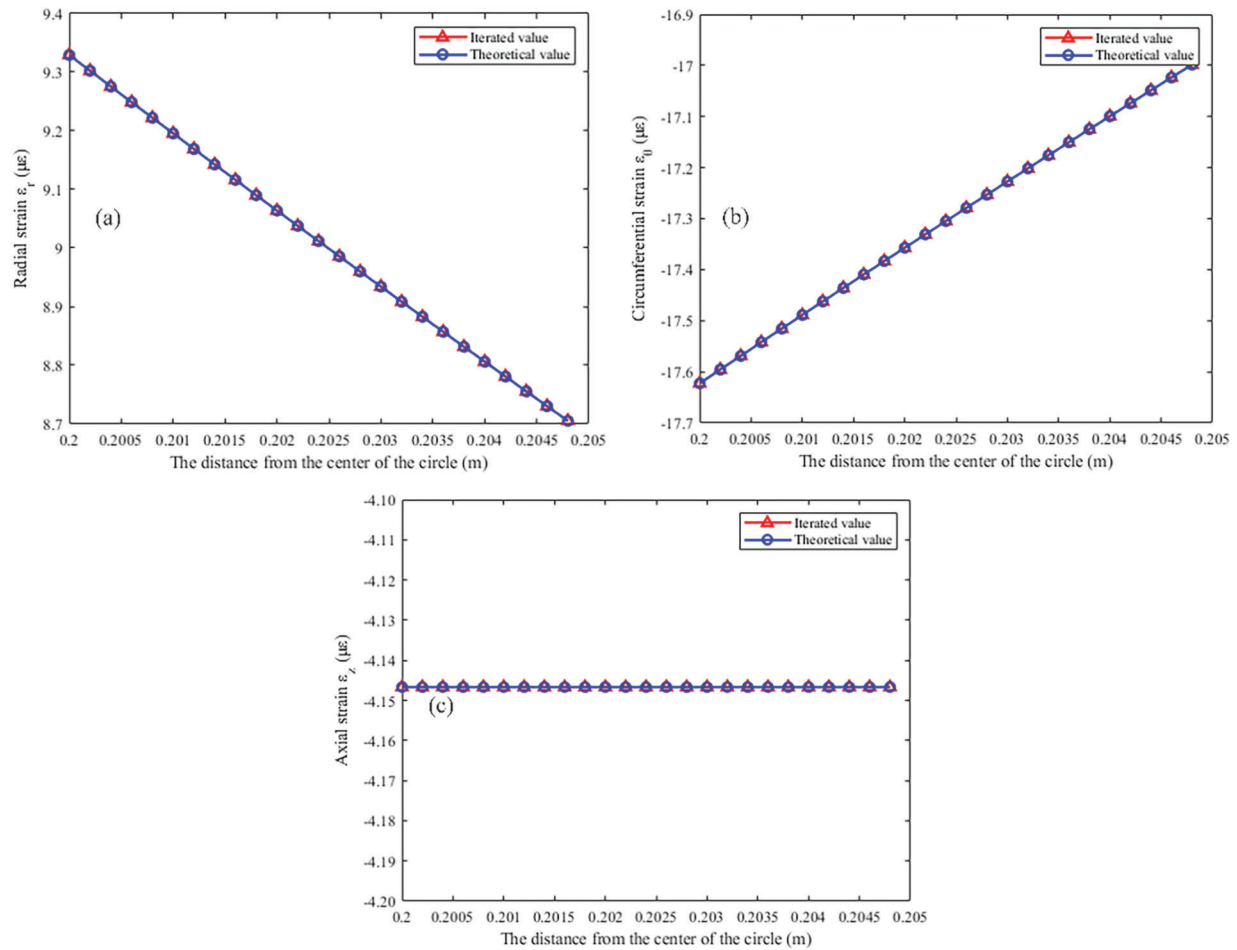

Figure 10: Comparison of iterative solution and theoretical solution: (a) Radial strain; (b) Circumferential strain; (c) Axial strain

According to the structural characteristics of the vacuum vessel and the possible leakage location, the quasi-distributed FBG sensors have been selected to be arranged in the upper, middle and lower layers near the valve. Given that the vacuum vessel structure experiences shrinkage deformation due to the negative pressure during the vacuum process, two kinds of quasi-distributed FBGs in series (flexible packaged and bare FBG sensors) are selected to measure the variation information of the structural stress state during the vacuum process. The flexible packaging material is a silicone elastomer formed by mixing and curing SYLGARD 184 silicone elastomer base and SYLGARD 184 silicone elastomer curing agent with a proportion of 10:1. To minimize the deformation transfer effect due to the material differences of the intermediate media layers, SYLGARD 184 silicone elastomer mixture has been used to

adhere the FBGs in series to the vessel wall surface. The packaged 8-point FBG sensors (Pt-8FBGs), 6-point bare FBG sensors (B-6FBGs) and another packaged 8-point FBG sensor (Pb-8FBGs) have been pasted on the vacuum tank, respectively. The abbreviated "Pt" and "Pb" of Pt-8FBGs and Pb-8FBGs mean the packaged sensors located separately in the top and bottom positions of the vacuum vessel. In addition, a bare FBG (B-FBG-t) is serially connected at the end of the Pt-8FBGs sensor to assess the impact of the surrounding temperature. The FBG sensing elements have a reflectivity of 90%. The detailed sensor layout is shown in Fig. 11a, and the sensing test system is shown in Fig. 11b. The physical diagram of the optical fiber demodulator and its correlated parameters are shown in Fig. 12.
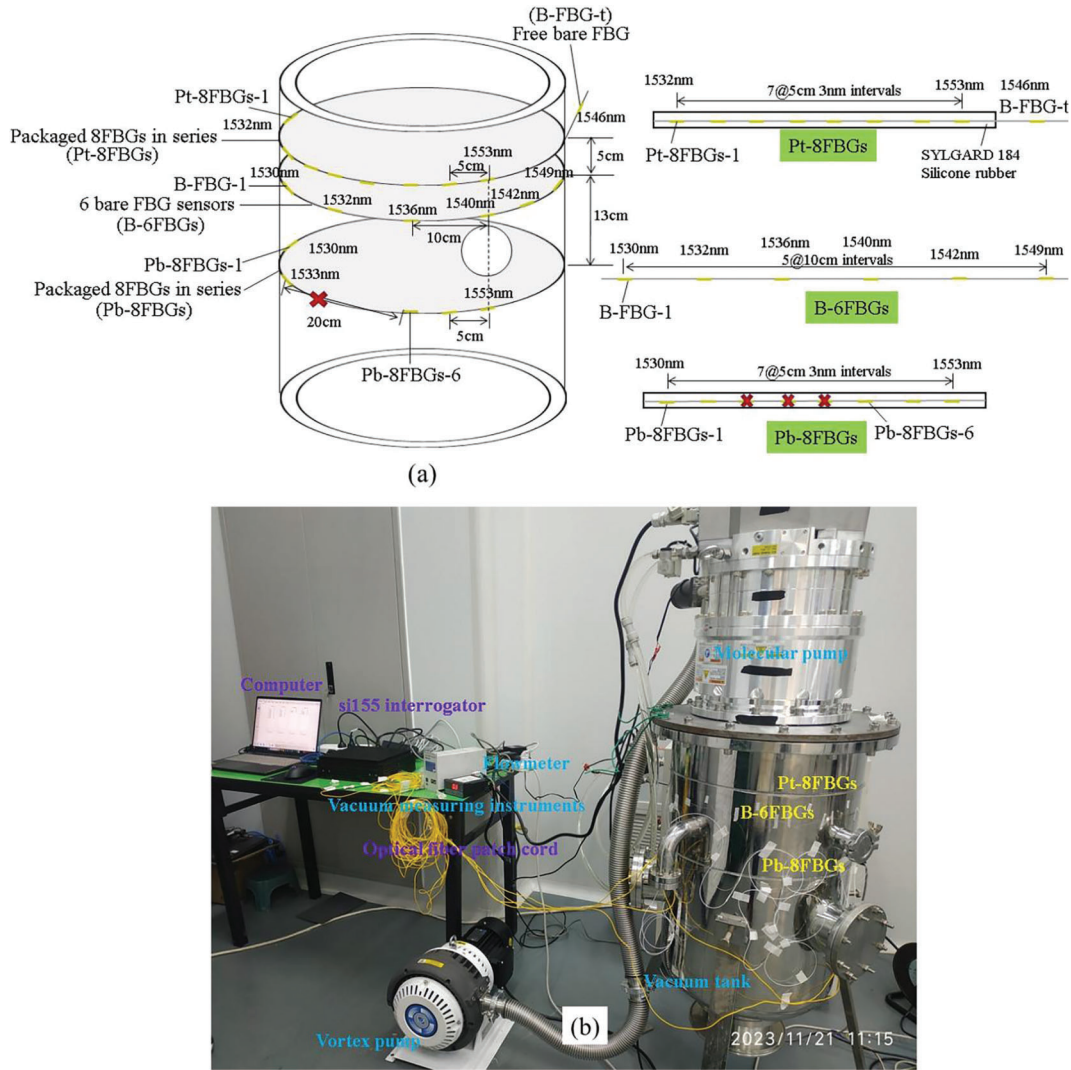

Figure 11: Vacuum process monitoring system of the vacuum tank: (a) Sensor layout; (b) Testing device

The sensor B-FBG-t, which is used to measure the effects of ambient temperature, had a minimal change in wavelength from 9:54 am on 29 November to 9:55 am on 30 November, as shown in Fig. 13. When the temperature effect can be ignored, the strain can be expressed as:

$$\varepsilon = \frac{\Delta \lambda_B}{\lambda_B k_\varepsilon} \tag{26}$$

where λ_B is the central wavelength of FBG, $\Delta\lambda_B$ is the central wavelength increment and k_ε is the strain sensitivity coefficient. It should be noted that the value of $\lambda_B k_\varepsilon$ is about 1.2 pm/με.
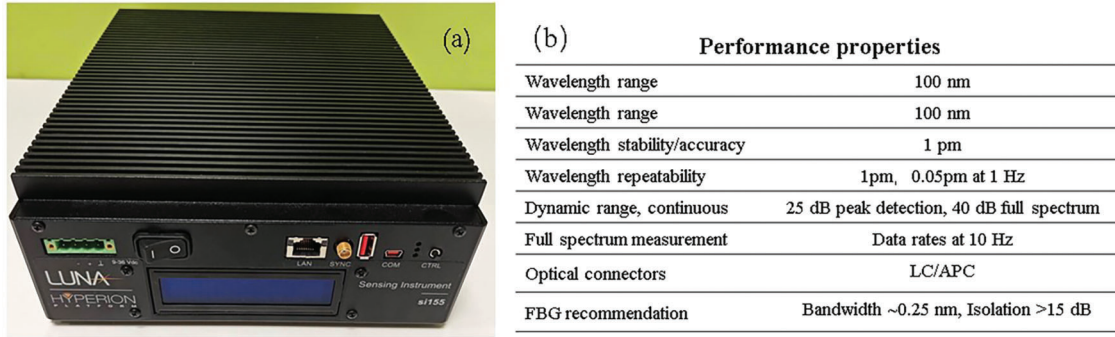

(b)	Performance properties
Wavelength range	100 nm
Wavelength range	100 nm
Wavelength stability/accuracy	1 pm
Wavelength repeatability	1pm, 0.05pm at 1 Hz
Dynamic range, continuous	25 dB peak detection, 40 dB full spectrum
Full spectrum measurement	Data rates at 10 Hz
Optical connectors	LC/APC
FBG recommendation	Bandwidth ~0.25 nm, Isolation >15 dB

Figure 12: Optical fiber demodulator: (a) Physical photo; (b) Performance parameters
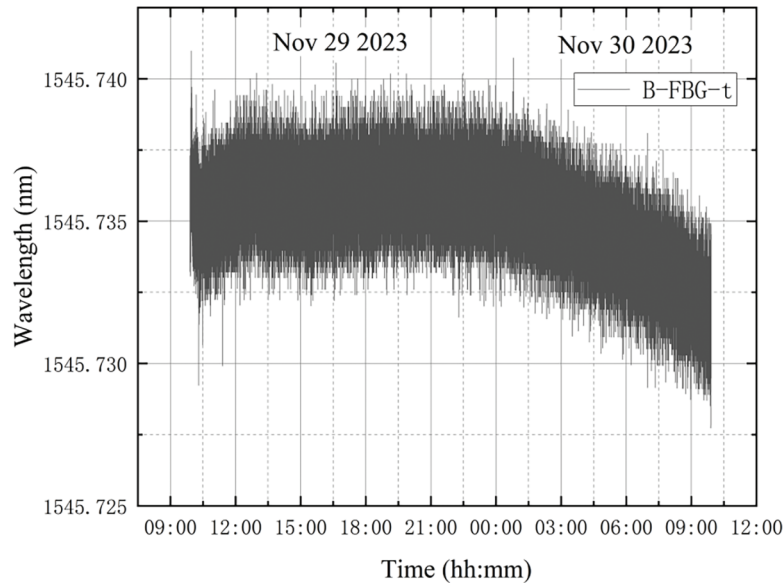

Figure 13: Wavelength variation of the measurement point in sensor B-FBG-t

3.2 Analysis on Monitoring Data

3.2.1 The First Testing

The loading process started on 21 November, and the initial values of the FBG sensors were firstly measured from 11:13 am for a duration of five minutes. The stabilized wavelength was taken as the initial wavelength. The vacuum extraction process using the vortex pump began at 11:19 am, at which point the flowmeter was shut off. At 11:58 am, the vortex pump was turned off, natural pressurization started, and the vessel's internal pressure was 1.95 Pa. The test proceeded until 12:30 pm, by which time the internal pressure had risen to 4.3 Pa. The test was paused due to a power outage. When it resumed at 3:34 pm, the internal pressure of the vessel was 9.46 Pa. The test continued until 9:20 am on 22 November, by

which time the vessel pressure had risen to 19.5 Pa. At 9:44 am, the valve was opened, causing the internal pressure of the vessel to return to the standard atmospheric pressure. The wavelength trend of the first measurement point of the three numbered sensors over time is shown in Figs. 14–17. Among them, Pb-8FBGs-12 is the first two measurement points of the sensor Pb-8FBGs, and Pb-8FBGs-678 is the last three measurement points of the sensor Pb-8FBGs.
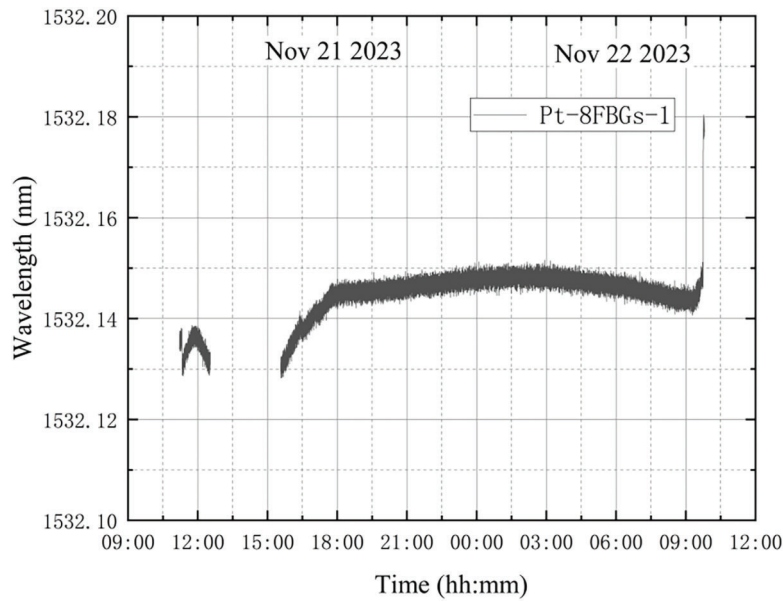

Figure 14: Wavelength variation of the first measurement point in sensor Pt-8FBGs
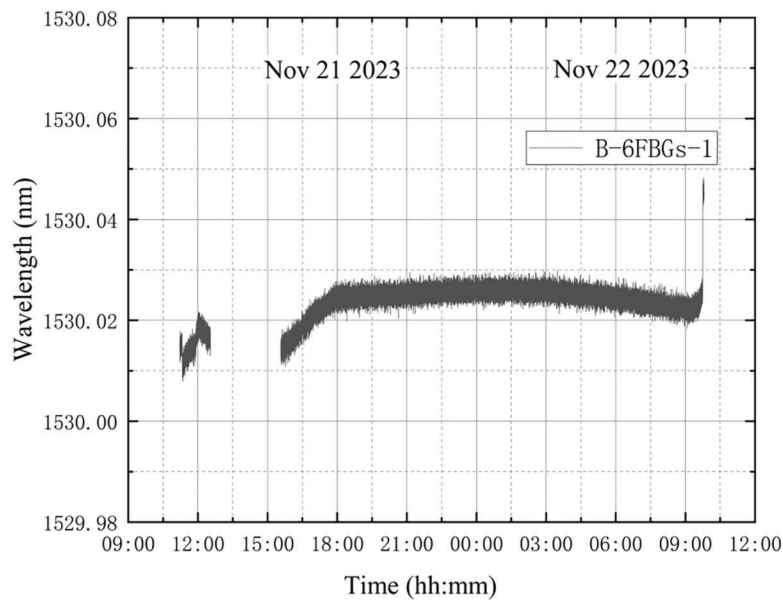
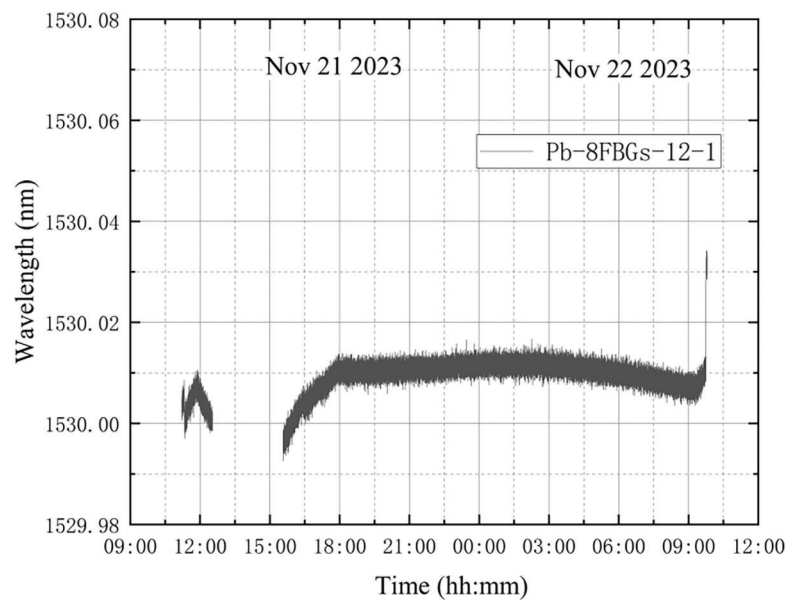**Figure 15:** Wavelength variation of the first measurement point in sensor B-6FBGs

Figure 16: Wavelength variation of the first measurement point in sensor Pb-8FBGs-12
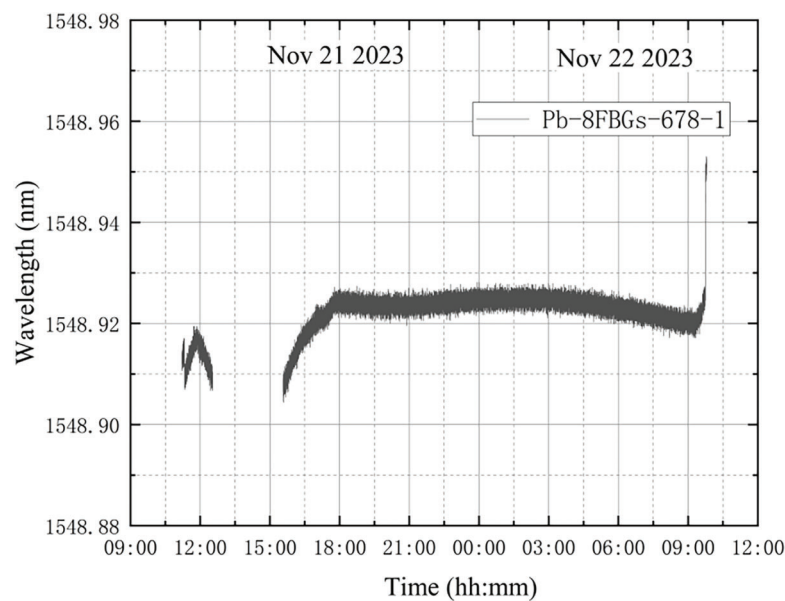

Figure 17: Wavelength variation of the first measurement point in sensor Pb-8FBGs-678

It is evident that the wavelength variations at the four FBG measurement points follow similar trends. After measuring the initial values at 11:18 am on 21 November, vacuum extraction of the vacuum tank began. Due to the efficient vacuum extraction by the vortex pump, the pressure inside the tank dropped quickly from the standard atmospheric pressure. The tank was always under standard atmospheric pressure, which made the tank compressive. This caused the decreased wavelength of the FBGs. The

wavelength profiles in Figs. 14–17 all showed a steep drop at the start of vacuum extraction, indicating that the FBG sensor was highly sensitive to sudden variations of the pressure vessel. The wavelengths all maintained an increasing trend from 3:34 pm on 21 November to 3:00 am on 22 November, consistent with the actual slow increase of pressure in the tank after the vortex pump was turned off. At 9: 44 am on 22 November, the pressure in the vessel was immediately returned from 19.5 Pa to standard atmospheric pressure. Due to the sudden increase of pressure inside the tank, compressive action disappeared and the wavelength of FBG increased accordingly. The wavelength of FBG at each measurement point increased steeply when the valve was opened, indicating that the FBG sensor can effectively sense the vacuum loss process.

3.2.2 The Second Testing

After the first vacuum-loss test was completed, the pressure inside the vessel returned to standard atmospheric pressure. After the wavelength stabilized at 9:48 am on 22 November, the initial value of the FBG sensor began to be recorded. The recording time was about five minutes, and the average value could be used as the initial wavelength. Then, the second test continued. At 9:55 am, the vortex pump was activated for vacuum extraction, and the flowmeter was closed at that moment. The extraction process lasted until 5:04 pm, at which point the vortex pump was turned off, and the internal pressure of the vessel had reached 0.42 Pa. The flowmeter remained open but was not connected to the vessel, allowing natural pressurization to proceed. This process continued until 10:00 am on 23 November, by which time the internal pressure of the vessel had reached 225 Pa. At 10:01 am, the valve was opened, and the vessel's internal pressure gradually rose to standard atmospheric pressure. Figs. 18–21 show the FBG wavelength variations at the first measurement point of the three numbered sensors.
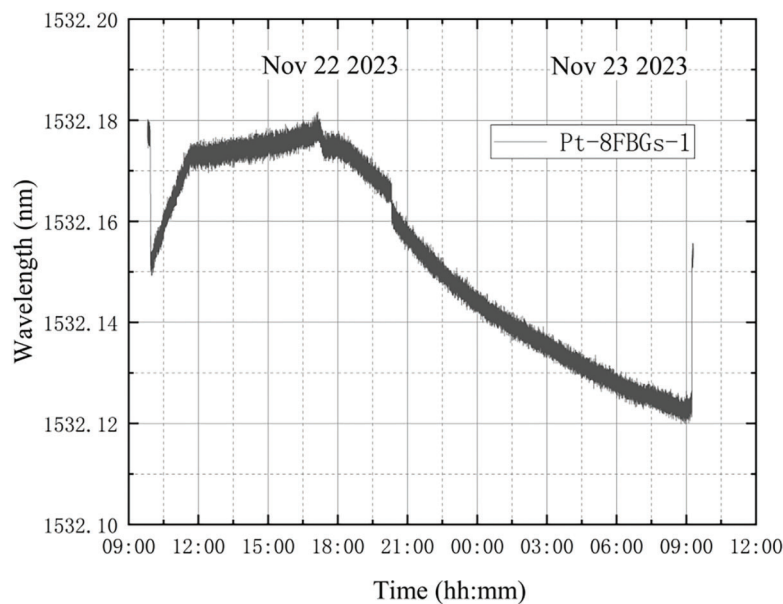

Figure 18: Wavelength variation of the first measurement point in sensor Pt-8FBGs

It is apparent that the variation trends of FBG wavelengths at the first measurement point of the three sensors are generally consistent, which indicates the high sensitivity of each FBG sensor at different positions to sense the structural state information of the pressure vessel during the whole vacuum pumping and vacuum loss process. After the vacuum was extracted by using the vortex pump, the pressure (equal to the standard atmospheric pressure) inside the tank decreased rapidly. The outside of the

tank always suffered from standard atmospheric pressure, which made the tank in compression and the attached FBG sensor with a reduced wavelength. The wavelengths of the FBGs at each measurement point show a steep drop at the beginning of the vacuum extraction, which is accorded with the mechanical law. When the valve was opened, the pressure inside the tank increased from 225 Pa directly to standard atmospheric pressure, which accordingly induced the increased wavelength of the FBG sensors. The wavelengths of FBGs at each measurement point had a steep increase when the valve was opened, indicating that the FBG sensor can accurately sense the mutation behavior of structural deformation.
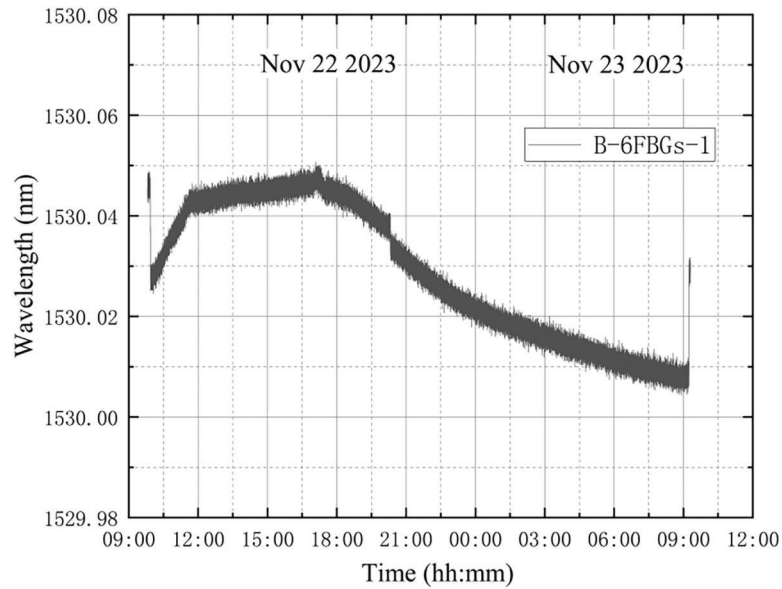

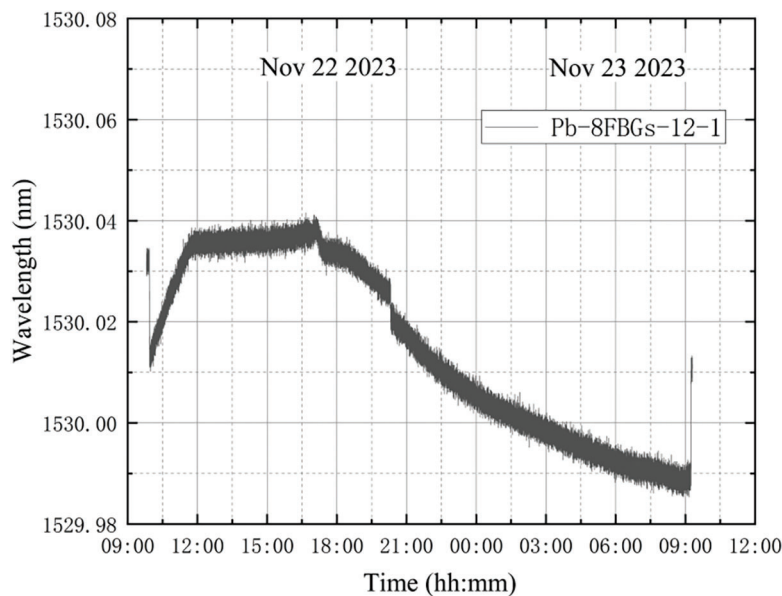**Figure 19:** Wavelength variation of the first measurement point in sensor B-6FBGs

Figure 20: Wavelength variation of the first measurement point in sensor Pb-8FBGs-12
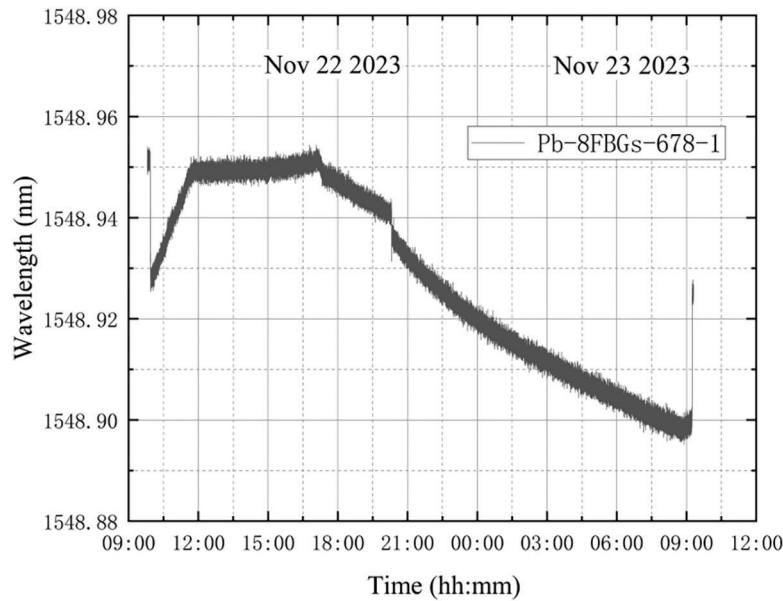
Figure 21: Wavelength variation of the first measurement point in sensor Pb-8FBGs-678

Compared to the first testing, the second testing opened the flowmeter during the natural pressurization process, and the pressure in the tank before opening the valve was 19.5 Pa with the flowmeter closed during the first testing, while the pressure in the tank before opening the valve with the flowmeter opened was 225 Pa during the second testing. It is apparent that opening the flowmeter may accelerate the gas flow rate and pressure variations, speeding up the natural pressurization process and producing different loading effects on the pressure vessel structure. As a result, the whole-process wavelength variation curves measured by the FBG sensors were significantly different. It also indicates that FBG sensors have the ability to sense micro variations in the pressure vessel structure with high accuracy and sensitivity.

3.2.3 The Third Testing

Following the second test, the initial values for each measurement point of the FBG sensors were recorded for approximately 5 min, beginning at 10:05 am on 23 November, once the wavelengths had stabilized. The average value was used as the initial wavelength for the third test. The vortex pump was activated at 10:11 am, and the flowmeter was still closed. The molecular pump can be activated once the pressure drops below 30 Pa. It is important to note that both the molecular pump and the vortex pump must be operating at the same time. The molecular pump generally evacuates the air by using a vane in the upper of the vessel and then the air is discharged through the pipe. The molecular pump was turned on at 10:14 am and gradually turned off starting at 5:38 pm, with the internal pressure of the vessel reaching 2.45 Pa. At 5:49 pm, the molecular pump was completely switched off, and the vortex pump was closed simultaneously. Natural pressurization began, and the flowmeter was also left open. When the vortex pump was closed at 9:01 am on 24 November, the pressure in the vessel was 144 Pa. The molecular pump was removed from the vessel at 9:15 am, which made the pressure in the vessel gradually increase to the standard atmospheric pressure. The testing ended at 9:56 am on 24 November. Throughout the loading and unloading process, the wavelength changes of the first measurement point in each FBG sensor as shown in Figs. 22–25.

It is apparent that the variation trends of wavelengths of FBGs at each measurement point are generally consistent. Due to the use of a vortex pump for extracting the vacuum, the pressure inside the tank decreased rapidly from standard atmospheric pressure. The tank suffered from shrinkage deformation under the

pressures, resulting in the wavelength reduction of the FBG sensors attached to the tank. The wavelengths of the FBGs at each measurement point show a steep drop at the beginning of the vacuum extraction, which is accorded with the mechanical law. When the molecular pump was disassembled at 9:01 am on 24 November, the pressure inside the tank returned to standard atmospheric pressure, and the pressurization was no longer present. The wavelength of each FBG thus increased accordingly, and a steep increase occurred when the valve was opened, which is consistent with the law of structural deformation.
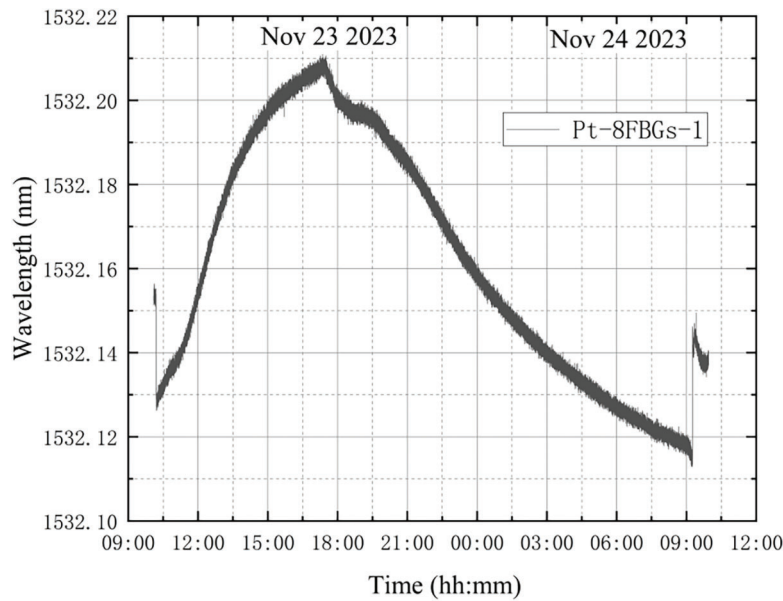
Figure 22: Wavelength variation of the first measurement point in sensor Pt-8FBGs
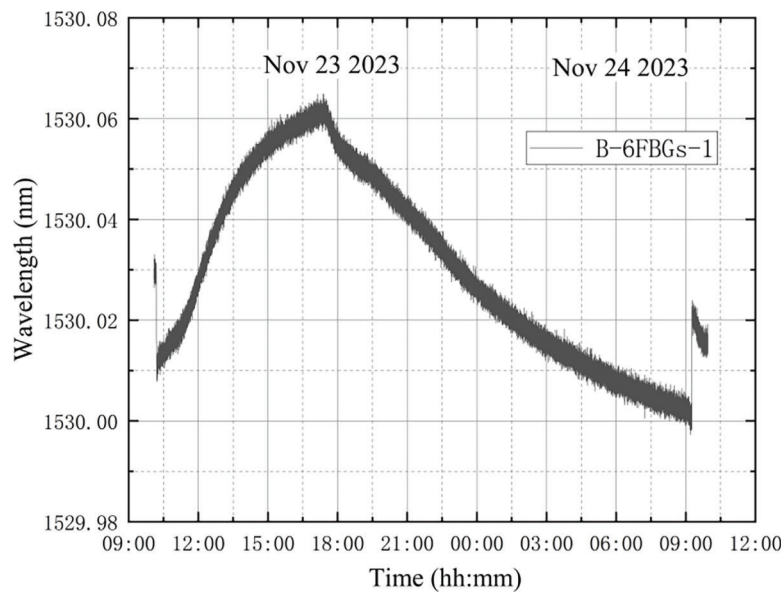
Figure 23: Wavelength variation of the first measurement point in sensor B-6FBGs
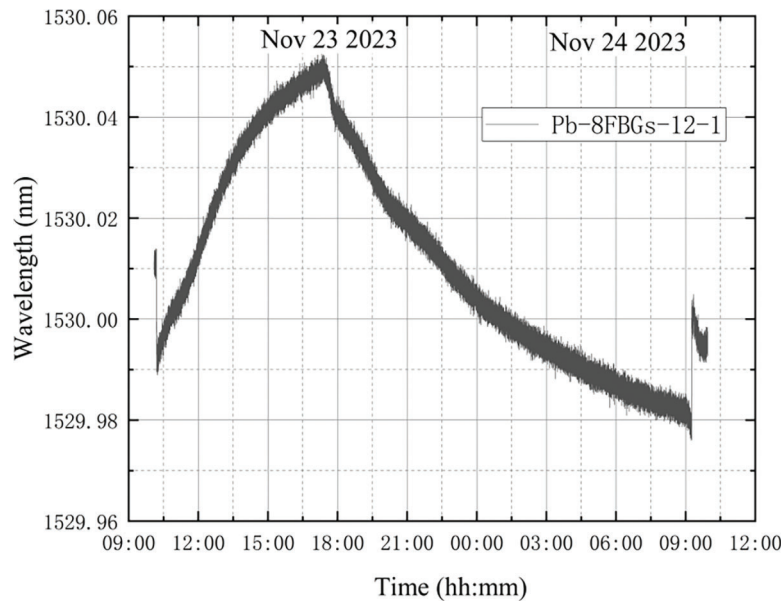
Figure 24: Wavelength variation of the first measurement point in sensor Pb-8FBGs-12
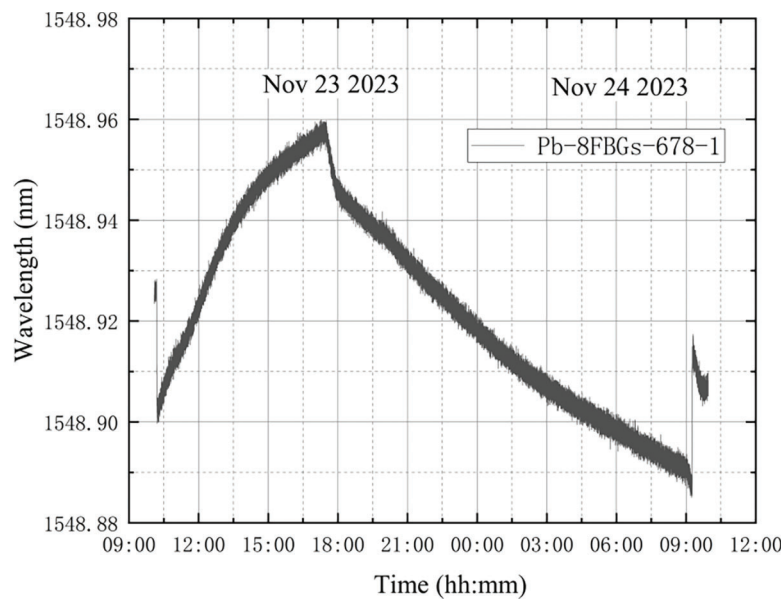

Figure 25: Wavelength variation of the first measurement point in sensor Pb-8FBGs-678

Comparing the second and third testing, it can be seen that a significant difference occurs in the deformation effects of the pressure vessel tank under different vacuum loading and unloading modes, but the tank structure undergoes a mutation effect at both the vacuum loading and unloading moments. When using a vortex pump and molecular pump to extract vacuum simultaneously, the deformation generated by the structure is larger. Besides, it also verifies that the FBG sensors can accurately and sensitively reflect the microstrain variation of the pressure vessel structure.

3.3 Discussion

Combining the observation of the images of the three experiments with the theoretical analysis, it was found that all parts of the images differed a little from the theoretical expectations, except for the moments when vacuum extraction started and the pressure inside the tank was returned to standard atmospheric pressure. During continuous vacuum extraction, the pressure inside the tank continues to drop, resulting in a gradually increasing pressure difference between the inside and outside of the tank. According to the theoretical expectation, the tank is continuously pressurized during the process, and the wavelength of FBG at each measurement point will continue to decrease during the process. When the pressure inside the tank gradually approaches the power limit of the vortex pump and molecular pump, the decreasing trend of wavelength may become slow or stabilize. However, it is found that at some moments the wavelength actually shows an increasing trend in the second and third experiments, which is opposite to the expected variations. Meanwhile, during natural pressurization, although the pressure difference between the inside and outside of the tank still exists, with the slow increase of the pressure inside the tank, it is theorized that the wavelengths of FBG at each measurement point should show a slow increase or a relatively stable trend. However, the experimental images show that the wavelength continues to decrease during natural pressurization, which is inconsistent with the theoretically expected results.

According to further temperature experimental testing analysis by excluding the temperature influence [21,22], it was found that the loading and unloading process of the operation of the pump generated vibration, resulting in the pressure vessel tank micro-vibration. The deformation produced by this vibration effect was larger than the shrinkage deformation caused by the negative pressure, which led to the phenomenon of increasing wavelength values after vacuum extraction [23]. In the first experiment, the growing trend of the wavelength suddenly stopped or slowed down at 12:00 am on 21 November, which was caused by the vibration stop of the tank due to the shutdown of the vortex pump at this point. In the second experiment, the wavelength should ideally have remained on a declining trend, except for the steep drop at the beginning. However, this declining trend did not occur until after the vortex pumps were shut down at 5:04 pm on 22 November, and the wavelength gradually declined to normal values after the vortex pumps were shut down. The change in wavelength at 12:00 am on 22 November. in the second experiment may be due to a delayed response of the tank components caused by vibration. At 12:00 am the response of the tank components stabilized, and the wavelength increase slowed down. The increase in pressure in the tank between 5:04 pm on 22 November and 10:01 am on 23 November. was quite slow, and the wavelength did not show a slow upward trend. The same situation occurred in the third experiment. In the third experiment, it was not until the vortex pump was turned off at 5:38 pm on 23 November. that the wavelength showed a downward trend. It can be seen that the vibration effect generated by the operation of the vortex pump and molecular pump during vacuum loading and unloading processes is more pronounced than the negative pressure effect when the vacuum-induced shrinkage deformation of the tank is small. In monitoring the whole vacuum process, it is necessary to consider the removal of the influence of this factor in order to accurately obtain the variation characteristics of the tank caused by the vacuum loss [24,25]. In the three experiments, the FBG sensors show high accuracy and sensitivity in sensing the micro variations of the pressure vessel tank structure, which further indicates that the proposed FBG sensing technology has the potential to monitor the micro defect and leakage of vacuum pressure vessels.

4 Conclusion

To develop an efficient method for the online vacuum loss process monitoring, the theoretical and numerical analysis of the vacuum pressure vessel structures under different internal and external pressures has been explored, and three kinds of testing on the practical pressure vessel equipped with designed FBG sensors under different loading and unloading modes have also been conducted. Based on the study, the following conclusions can be drawn:

(1) The theoretical analysis provides straightforward formulas to declare the stress and strain variations of circular pressure vessel structures under different internal and external pressures, which can provide instructions for the configuration of the monitoring system for the vacuum loss process identification. The numerical analysis based on the iteration method has also been given to support the effectiveness of the theoretical analysis, which can be further used to explore the complicated case that the pressure vessel with a micro defect is subjected to internal and external pressures.

(2) According to the collected continuous monitoring data, the stress and strain distributions of the pressure tank during the vacuum loss process under different loading modes can be much more accurately recognized based on the FBG sensors. It verifies the effectiveness of the proposed monitoring method and provides suggestions for the improvement of an accurate, simple, fast, and online identification system to characterize the long-term structural performance, vacuum loss process, and leakage of vacuum pressure vessel structures.

(3) The testing results indicate that the microstrain induced by the loading vibration of the vortex pump and the molecular pump plays a high weight on the measured signals during the vacuum extraction and loss processes. It is thus particularly important to consider the feasible measure to control the loading mode inducted vibration of the pressure vessels, to keep the long-term health and service of the pressure vessels. The signal filtering technique should be also considered to separate the abnormal information and recognize the true features induced by vacuum loss.

Author Contributions: Zhe Gong participated in the experiments, organized and maintained the research data, deduced the theoretical knowledge; Ge Yan: experimental design, providing laboratory resources, participating in experiments; Jie Ma participated in experiments, organized and analyzed experimental data; Chang-Lin Yan: experimental design, providing laboratory resources, participating in experiments; Fu-Kang Shen participated in the experiments; Hu Li: experimental design, managing and coordinating the experimental program; Hua-Ping Wang proposed experimental ideas and participated in experiments, paper conceptualization and writing, paper review. All authors reviewed the results and approved the final version of the manuscript.

Availability of Data and Materials: The authors confirm that the data supporting the results of this study are available in the article.

Ethics Approval: Not applicable.

Conflicts of Interest: The authors declare no conflicts of interest to report regarding the present study.

References

1. Chen XD, Fan ZC, Chen YD, Xu SQ, Cui J, Zhang XX, et al. Technological progress on design, manufacturing and maintenance of high-end pressure vessels in China. J Mech Eng. 2023;59(20):18–33. doi:10.3901/JME.2023.20.018.
2. Gao D, Wu Z, Yang L, Zheng Y, Yin W. Structural health monitoring for long-term aircraft storage tanks under cryogenic temperature. Aerosp Sci Technol. 2019;92:881–91. doi:10.1016/j.ast.2019.02.045.

3. Zhou W, Wang J, Pan ZB, Liu J, Ma LH, Zhou JY. Review on optimization design, failure analysis and non-destructive testing of composite hydrogen storage vessel. Int J Hydrogen Energy. 2022;47(91):38862–83. doi:10.1016/j.ijhydene.2022.09.028.

4. Kinet D, Chah K, Gusarov A, Faustov A, Areias L, Troullinos I, et al. Proof of concept for temperature and strain measurements with fiber bragg gratings embedded in supercontainers designed for nuclear waste storage. IEEE Trans Nucl Sci. 2016;63(3):1955–62. doi:10.1109/TNS.2016.2555337.

5. Yaacoubi S, McKeon P, Ke W, Declercq NF, Dahmene F. Towards an ultrasonic guided wave procedure for health monitoring of composite vessels: application to hydrogen-powered aircraft. Materials. 2017;10(9):1097–7. doi:10.3390/ma10091097.

6. Graue R, Krisson M, Erdmann M, Reutlinger A. Integrated health monitoring approach for reusable cryogenic tank structures. J Spacecr Rockets. 2000;37(5):580–5. doi:10.2514/2.3630.

7. Tra V, Duong BP, Kim JY, Sohaib M, Kim JM. Improving the performance of storage tank fault diagnosis by removing unwanted components and utilizing wavelet-based features. Entropy. 2019;21(2):145. doi:10.3390/e21020145.

8. Ansari F. Practical implement of optical fiber sensors in civil structural health monitoring of bridges. J Intell Mater, Syst Struct. 2007;18(8):879–89. doi:10.1177/1045389X06075760.

9. Wang HP, Xiang P, Jiang LZ. Strain transfer theory of industrialized optical fiber-based sensors in civil engineering: a review on measurement accuracy, design and calibration. Sens Actuators A. 2019;285(2):414–26. doi:10.1016/j.sna.2018.11.019.

10. Lo YL, Sung PH, Wang HJ, Chen LW. Pressure vessel wall thinning detection using multiple pairs of fiber bragg gratings for unbalanced strain measurements. J Nondestruct Eval. 2000;19(3):105–13. doi:10.1023/A:1026575024826.

11. Latka I, Ecke W, Höfer B, Chojetzki C, Reutlinger A. Fiber optic sensors for the monitoring of cryogenic spacecraft tank structures. In: Photonics North 2004: Photonic Applications in Telecommunications, Sensors, Software, and Lasers, 2004; Ottawa, ON, Canada. doi:10.1117/12.567353.

12. Mizutani T, Takeda N, Takeya H. On-board strain measurement of a cryogenic composite tank mounted on a reusable rocket using FBG sensors. Struct Health Monit. 2006;5(3):205–14. doi:10.1177/1475921706058016.

13. Tapeinos IG, Rajabzadeh A, Zarouchas DS, Stief M, Groves RM, Koussios S, et al. Evaluation of the mechanical performance of a composite multi-cell tank for cryogenic storage: part II—experimental assessment. Int J Hydrogen Energy. 2019;44(7):3931–43. doi:10.1016/j.ijhydene.2018.12.063.

14. Liang ZH, Liu DB, Wang X, Zhang J, Wu HQ, Qing XL, et al. FBG-based strain monitoring and temperature compensation for composite tank. Aerosp Sci Technol. 2022;127:107724. doi:10.1016/j.ast.2022.107724.

15. Wang HP, Chen C, Ni YQ, Jayawickrema M, Epaarachchi J. Computer-aided feature recognition of CFRP plates based on real-time strain fields reflected from FBG measured signals. Compos, Part B. 2023;263:110866. doi:10.1016/j.compositesb.2023.110866.

16. Karapanagiotis C, Schukar M, Krebber K. Distributed fiber optic sensors for structural health monitoring of composite pressure vessels. tm-Tech Mess. 2024;91(3–4):168–79.

17. Souza G, Tarpani JR. Using OBR for pressure monitoring and BVID detection in type IV composite overwrapped pressure vessels. J Compos Mater. 2021;55(3):423–36. doi:10.1177/0021998320951616.

18. Wang HP, Jiang LZ, Xiang P. Improving the durability of the optical fiber sensor based on strain transfer analysis. Opt Fiber Technol. 2018;42:97–104. doi:10.1016/j.yofte.2018.02.004.

19. Werlink RJ, Pena F. NASA prototype all composite tank cryogenic pressure tests to failure with structural health monitoring. In: International Workshop on Structural Health Monitoring, 2015; San Francisco, CA, USA.

20. Lazaro RC, Souza E, Frizera A, Marques C, Frizera A. Optical fiber sensors systems in oil tanks: toward structural health monitoring and liquid-level estimation. IEEE Sens J. 2023;10:10437–43.

21. Sampath U, Kim D, Kim H, Song M. Polymer-coated FBG sensor for simultaneous temperature and strain monitoring in composite materials under cryogenic conditions. Appl Opt. 2018;57(3):492–7. doi:10.1364/AO.57.000492.

22. Wang HP, Dai JG, Wang XZ. Improved temperature compensation of fiber Bragg grating-based sensors applied to structures under different loading conditions. Opt Fiber Technol. 2021;63:102506. doi:10.1016/j.yofte.2021.102506.

23. Guyo ED, Hartmann T. Evaluating the efficiency and performance of data persistent systems in managing building and environmental data: a comparative study. Adv Eng Inform. 2024;62:102582. doi:10.1016/j.aei.2024.102582.

24. Ma J, Gong Z, Yan CL, Cao PF, Wang HP. Wavelet denoising analysis on vacuum-process monitoring signals of aerospace vacuum vessel structures. Meas Sci Technol. 2024;35(12):126008. doi:10.1088/1361-6501/ad7481.

25. Golmohammadi A, Hasheminejad N, Hernando D, Vanlanduit S, Van den bergh W. Performance assessment of discrete wavelet transform for de-noising of FBG sensors signals embedded in asphalt pavement. Opt Fiber Technol. 2024;82:103596. doi:10.1016/j.yofte.2023.103596.